Frictional strength heterogeneity and surface heat flow: Implications for the strength of the creeping San Andreas fault

M. A. d'Alessio,[1] C. F. Williams,[1] and R. Bürgmann[2]

Received 13 April 2005; revised 24 January 2006; accepted 15 February 2006; published 31 May 2006.

[1] Heat flow measurements along much of the San Andreas fault (SAF) constrain the apparent coefficient of friction (μ_{app}) of the fault to <0.2, much lower than laboratory-derived friction values for most geologic materials. However, heat flow data are sparse near the creeping section of the SAF, a frictional "asperity" where the fault slips almost exclusively by aseismic creep. We test the hypothesis that the creeping section has a substantially higher or lower μ_{app} than adjacent sections of the SAF. We use numerical models to explore the effects of faults with spatially and temporally heterogeneous frictional strength on the spatial distribution of surface heat flow. Heat flow from finite length asperities is uniformly lower than predicted by assuming an infinitely long fault. Over geologic time, lateral offset from strike-slip faulting produces heat flow patterns that are asymmetric across the fault and along strike. We explore a range of asperity sizes, slip rates, and displacement histories for comparing predicted spatial patterns of heat flow with existing measurements. Models with $\mu_{app} \sim 0.1$ fit the data best. For most scenarios, heat flow anomalies from a frictional asperity with $\mu_{app} > 0.2$ should be detectable even with the sparse existing observations, implying that μ_{app} for the creeping section is as low as the surrounding SAF. Because the creeping section does not slip in large earthquakes, the mechanism controlling its weakness is not related to dynamic processes resulting from high slip rate earthquake ruptures.

Citation: d'Alessio, M. A., C. F. Williams, and R. Bürgmann (2006), Frictional strength heterogeneity and surface heat flow: Implications for the strength of the creeping San Andreas fault, *J. Geophys. Res.*, *111*, B05410, doi:10.1029/2005JB003780.

1. Introduction

[2] The frictional strength of faults controls the amount of frictional heat generated during slip. Direct observations of the surface heat flow distribution near active faults theoretically can detect this heat and therefore provide insight into the mechanics of faulting. Existing heat flow analyses rely on models of infinitely long faults with uniform friction, but it is unlikely that natural faults have uniform friction throughout. For example, *Brune* [2002] noted that the creeping section of the San Andreas fault (SAF) has not produced large earthquakes, so its mechanical behavior is not altered by processes that occur during dynamic earthquake rupture. These processes tend to reduce frictional strength (section 1.2), so he suggested that the creeping section has a higher frictional strength than the surrounding portions of the fault (i.e., it is a frictional asperity). Asperities will produce heat flow patterns that are more complicated than infinitely long faults, but this effect has not been properly quantified. We develop the theoretical framework for calculating the spatial and temporal distribution of frictional heat about finite frictional asperities. We then test Brune's hypothesis about the strength of the creeping section and explore the implications for the mechanisms that control fault strength.

1.1. Stress–Heat Flow Debate

[3] Our understanding of fault friction is based on laboratory experiments that show that the coefficient of friction (μ_{app}) is >0.6 for almost all geologic materials [*Byerlee*, 1978]. However, these experiments may be neglecting crucial processes that control friction at the scale of large faults in nature. Evidence from surface heat flow [*Brune et al.*, 1969; *Lachenbruch and Sass*, 1980], thermochronology [*Xu and Kamp*, 2000; *d'Alessio et al.*, 2003], and the orientation of the maximum principal stress [*Mount and Suppe*, 1987; *Hardebeck and Hauksson*, 1999; *Provost and Houston*, 2001; *Hickman and Zoback*, 2004; *Townend and Zoback*, 2004] all suggest that the average coefficient of friction of the SAF and possibly other large faults could be 0.2 or lower (a "weak fault"). While such studies are intriguing, similar data also have been used to argue that natural faults have frictional properties quite similar to laboratory measurements ($\mu_{app} > 0.6$, a "strong fault") [*Scholz et al.*, 1979; *Camacho et al.*, 2001; *Scholz*, 2000; *Castillo and Hickman*, 2000; *Townend and Zoback*, 2000], or have intermediate frictional strength [*Hardebeck and*

[1]U.S. Geological Survey, Menlo Park, California, USA.
[2]Department of Earth and Planetary Science, University of California, Berkeley, California, USA.

0148-0227/06/2005JB003780$09.00

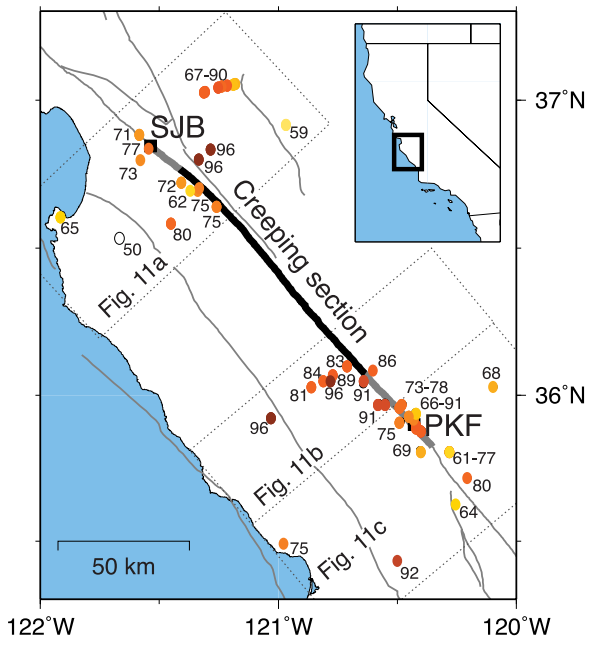

Figure 1. Creeping section of the San Andreas fault. Labeled symbols are existing heat flow measurements in mW m^{-2} (Table 1). Thick black line indicates where the SAF is thought to be freely slipping, thick grey lines are transition zones between creeping and locked behavior. Thin lines are all active faults. Dotted boxes show subregions (Figure 11 and Table 3). SJB, San Juan Bautista; PKF, Parkfield.

Michael, 2004]. These conflicting results highlight the fact that fault friction is a complex property that may depend on many factors [also see *Lockner and Beeler*, 2002; *Scholz and Hanks*, 2004].

1.2. Dynamic Versus Persistent Weakness

[4] Researchers have proposed a number of physical mechanisms to explain the apparent weakness of natural faults. These mechanisms fall into two general categories: (1) dynamic (resulting from events related to the rupture process of large earthquakes) and (2) persistent (structural or lithologic features of the fault). Dynamic weakening mechanisms result in reduced effective normal stress on the fault during rapid slip. The reduction in normal stress can be achieved by interface separation [*Brune et al.*, 1993], acoustic fluidization of fault zone materials [*Melosh*, 1996], or earthquake-induced thermal expansion of pore fluids [*Lachenbruch*, 1980; *Mase and Smith*, 1987; *Andrews*, 2002]. Unlike dynamic weakening mechanisms that only impact the fault zone during high slip rate earthquakes, "persistent" weakening mechanisms require structural or lithologic features that persist throughout the entire earthquake cycle within a fault zone. Serpentinite gouge [*Moore et al.*, 1996, 2004] and illite and smectite clays [*Morrow et al.*, 1992; *Brown et al.*, 2003] are frictionally weak under certain pressure and temperature conditions and could weaken fault zones. Similarly, low-permeability structures would permit consistently elevated pore pressures in the fault zone, especially if there is a constant source of fluids [e.g., *Irwin and Barnes*, 1975; *Rice*, 1992]. Given the range of plausible weakening mechanisms, it is challenging to determine which processes are the most important in controlling the strength of natural faults. Existing analyses do not even distinguish which broad category of weakening dominates (dynamic versus persistent).

1.3. Creeping Section

[5] The creeping section of the SAF, where nearly all of the slip is accommodated by relatively steady, aseismic creep, provides an ideal natural laboratory for discriminating between dynamic and persistent weakness. The creeping section is a 160- to 170-km-long portion of the fault located in central California between San Juan Bautista and Parkfield (Figure 1) that rarely, if ever, experiences large earthquakes, in stark contrast to sections of the fault to the north (1906 San Francisco rupture extent) and to the south (1857 Fort Tejon rupture extent) that have produced repeated large earthquakes. This unique behavior reflects frictional properties of the fault that promote stable sliding [e.g., *Scholz*, 1998] and could also include a difference in frictional strength.

[6] If dynamic weakening from earthquake rupture exclusively controls fault strength, the creeping section must be frictionally strong because it slips without high slip rate earthquakes. *Brune* [2002] suggested that the creeping section has a higher μ_{app} than the rest of the SAF that surrounds it. While heat flow data constrain the coefficient of friction along much of the SAF, no heat flow observations have been collected along the central portion of the creeping section (Figure 1 and Table 1). Brune suggested that heat generated by this strong asperity might go undetected with the existing spatial distribution of measurements. Laboratory experiments show that a strong creeping section is physically possible because certain gouge minerals promote stable sliding (creep behavior) and have high coefficients of friction [*Brown et al.*, 2003].

1.4. Existing Formulations of Frictional Heat

[7] To constrain the coefficient of friction of the creeping section from surface heat flow measurements, we must be able to calculate the expected heat flow from finite length asperities.

[8] Quantifying the total frictional heat generated during fault slip involves complex feedbacks between heat generation, fluid pressure [*Lachenbruch*, 1980; *Mase and Smith*, 1987; *Andrews*, 2002], effective normal stress [*Brune et al.*, 1993; *Melosh*, 1996; *Brodsky and Kanamori*, 2001], melting [*McKenzie and Brune*, 1972], seismic wave generation [*McGarr*, 1999], frictional stability [*Blanpied et al.*, 1998], and other processes. To encompass all of these effects without regard to their detail or origin, the concept of an "apparent coefficient of friction" (μ_{app}) is frequently employed [*Harris*, 1998]. This quantity represents an average fault strength over the timescale of heat generation.

[9] Once heat is generated, it is transported away from the fault through both conductive and advective processes. Because of limited constraints on fluid pressures and permeabilities near active faults, there is debate over the role of fluid flow in advective heat transport around faults [*O'Neil and Hanks*, 1980; *Williams and Narasimhan*, 1989; *Saffer et al.*, 2003; *Fulton et al.*, 2004]. The recent studies suggest

Table 1. Heat Flow Observations and Uncertainties[a]

Site Code	Longitude, °E	Latitude, °N	HF, mW m^{-2}
PT5	−121.180	37.055	68 ± 5
PT6	−121.188	37.053	67 ± 10
PT3	−121.213	37.050	88 ± 4
PT2	−121.237	37.047	80 ± 6
PT9	−121.252	37.043	90 ± 9
PT0	−121.307	37.028	89 ± 10
PT1	−121.312	37.027	85 ± 5
HT7	−120.967	36.917	59 ± 6
HT2	−121.583	36.883	71 ± 7
SJBA	−121.545	36.837	77 ± 3
HT6	−121.283	36.833	96 ± 10
HT4	−121.333	36.800	96 ± 10
SJGD	−121.580	36.798	73 ± 4
HT1	−121.407	36.722	71 ± 1
LKA	−121.333	36.703	75 ± 2
LKC	−121.370	36.695	62 ± 6
LKB	−121.338	36.693	73 ± 3
STC	−121.258	36.640	75 ± 3
MOP	−121.915	36.605	65 ± 3
HT5	−121.450	36.583	80 ± 8
HT3	−121.667	36.533	50 ± 5
PR4	−120.708	36.095	83 ± 7
PDBV	−120.603	36.085	86 ± 9
PR3	−120.767	36.065	89 ± 13
US1	−120.781	36.050	96 ± 8
PR2	−120.812	36.050	84 ± 12
PRSN	−120.637	36.047	91 ± 8
PR1	−120.860	36.032	81 ± 5
KTL1	−120.100	36.030	68 ± 5
SFD1	−120.551	35.974	91 ± 3
PDSM	−120.579	35.972	91 ± 8
PPC2	−120.477	35.970	78 ± 7
VARN	−120.494	35.957	78 ± 8
PDL2	−120.423	35.941	66 ± 6
VARP	−120.447	35.927	73 ± 5
PAT	−121.028	35.925	96 ± 4
PDDL	−120.433	35.923	74 ± 7
FROL	−120.485	35.911	75 ± 8
EADE	−120.416	35.895	87 ± 7
EDE2	−120.422	35.894	83 ± 7
PHF2	−120.400	35.882	86 ± 8
PDHF	−120.395	35.879	91 ± 8
PDCH	−120.403	35.811	69 ± 20
PDSC	−120.282	35.810	61 ± 7
PSC2	−120.284	35.805	77 ± 9
PDJC	−120.205	35.716	80 ± 6
PDRH	−120.255	35.625	64 ± 4
HAR	−120.978	35.492	75 ± 8
TS1	−120.500	35.433	92 ± 3

[a]Sorted from north to south. Uncertainties are ±2 standard errors. From *Henyey* [1968], *Lachenbruch and Sass* [1980], *Williams et al.* [2004], and C. F. Williams (unpublished data, 2005).

that heat flow near the SAF is most consistent with heat flow dominated by conduction.

[10] The time and length scales of frictional heat anomalies cover wide ranges (hours to millions of years, centimeters to tens of kilometers [*d'Alessio et al.*, 2003]). *Lachenbruch* [1986] laid the framework for estimates of the localized effects of frictional heating in the days to months following an earthquake. These formulations were verified in laboratory work [*Lockner and Okubo*, 1983; *Blanpied et al.*, 1998], but there are few ways to directly test these heat flow models outside the laboratory. Thermochronology allows geologic searches for thermal signatures in both exhumed faults [*d'Alessio et al.*, 2003] and fault crossing boreholes [*Murakami et al.*, 2002]. Longer-timescale thermal anomalies near faults were well explored through surface heat flow [*Lachenbruch and Sass*, 1980]. To determine the temperature field near a fault with frictional heat generation, these authors begin with a solution to the conductive heat flow equation for a horizontal line source of heat in a half-space and integrate the line source over a range of depths [*Lachenbruch and Sass*, 1980, Appendix A]. The line source is infinitely long, resulting in infinitely long fault planes with homogeneous parameters along strike. Even though more complicated numerical models have been formulated to include the contribution of viscous shear heating in the lower crust [e.g., *Thatcher and England*, 1998; *Leloup et al.*, 1999; *Rolandone and Jaupart*, 2002], these models still restrict themselves to an infinitely long fault plane. While reasonable for many cases, this assumption does have its limitations.

[11] In the following sections, we introduce numerical models of purely conductive heat transport about finite length frictional asperities. We focus on examples with parameters similar to the creeping section of the SAF, but also discuss how results vary in more general cases. Our models therefore have implications for testing the strength of the creeping section as well as enhancing our broader understanding of spatial and temporal patterns of frictional heat anomalies from faults with heterogeneous friction.

2. Heat Flow Distribution About a Finite Asperity

[12] We explore the spatial and temporal distribution of temperature surrounding a rectangular fault patch in three dimensions. The fault patch is analogous to a high-friction asperity surrounded by frictionless sections. We focus on the case of a vertical strike-slip fault. Following *Lachenbruch and Sass* [1980], we allow for heat generation to be constant or to vary linearly with depth. While we assume constant heat generation along strike of each rectangular element, complex 3-D distributions of frictional asperities can be constructed as a series of these rectangular patches. We primarily use numerical models to calculate heat flow (section 3.1), but an analytical solution derived in the auxiliary material[1] exists for the single stationary asperity in this section. We have validated our numerical models with this analytic solution for cases where it applies.

[13] Figure 2 shows the distribution of surface heat flow for our reference model, a single frictional asperity 170 km long (the approximate length of the creeping section). We show the end member case of a very strong asperity ($\mu_{app} = 0.8$), but this result can be linearly scaled to represent faults with lower coefficients of friction (see Table 2 for model parameters). To highlight heating from the asperity, the rest of the fault along strike and below 15 km depth is frictionless and therefore generates no heat. This case was run until the surface heat flow distribution reached steady state. Overall, the map view of heat flow magnitude (Figure 2a) is similar to the infinite case near the midpoint of the surface trace of the asperity, but, as might be expected for a finite heat source, heat flow diminishes radially from the fault tips. The heat flow distribution is symmetric along strike and across the fault. Profiles perpendicular to the fault patch (Figures 2b–2d) are similar in shape to the infinitely long fault of *Lachenbruch and Sass* [1980], though peak heat flow magnitude near the asperity termination is lower than at the fault midpoint.

[1]Auxiliary material is available at ftp://ftp.agu.org/apend/jb/2005jb003780.

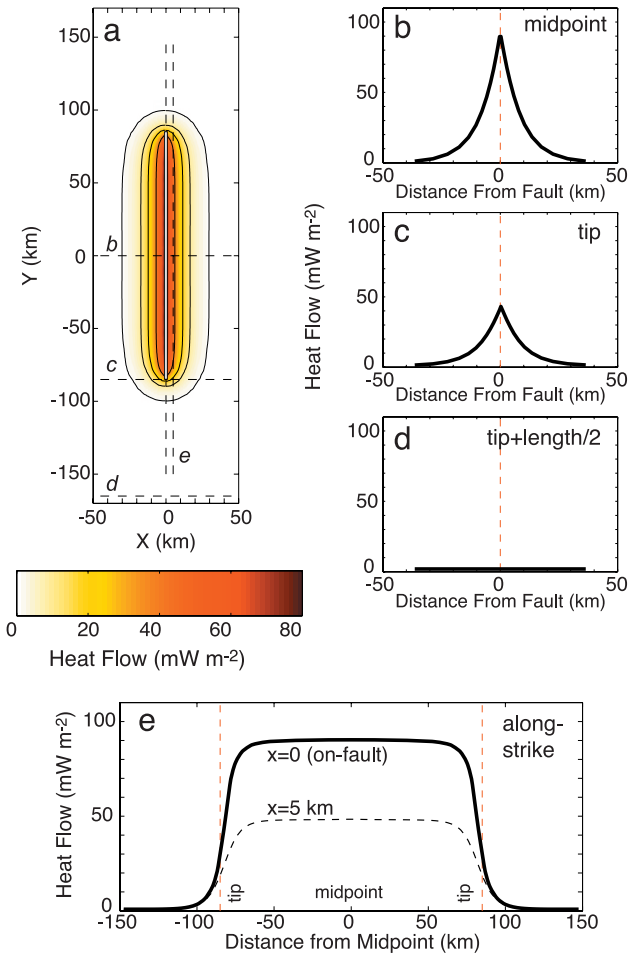

Figure 2. Steady state surface heat flow for our reference model, a single, vertical, rectangular asperity 170 km long extending to 15 km depth. (a) Map view distribution of heat flow. Approximate locations of profiles from Figures 2b–2e are shown as dashed lines. (b–d) Heat flow profiles taken perpendicular to the fault patch at its midpoint (Figure 2b), tip (Figure 2c), and one half the length of the fault trace beyond the tip (Figure 2d). (e) Heat flow profile along the strike of the fault patch.

[14] The profile along fault strike (Figure 2e) shows that heat flow drops proportionally to an error function centered at the fault tips (erf $[(y - y_{tip})/(\text{const})]$). Such a functional form implies that heat flow remains near its maximum value along much of the heat-generating fault surface. However, near the two ends of the fault, heat flow drops rapidly, with the values at the two ends equal to half the maximum value. For cases near steady state, the constant in the equation above depends strongly on the depth extent of fault heating and less so on the thermal diffusivity.

[15] Estimates of μ_{app} of a fault that assume an infinitely long fault could result in misinterpretation of sparse heat flow measurements. A high-friction asperity could be interpreted to be a uniformly weak fault with μ_{app} a factor of two lower than the actual μ_{app} if the constraining observations were located only near the endpoint of the heat generating asperity. The sparse data set of heat flow near the SAF is therefore prone to misinterpretation if friction is heterogeneous (see section 3.5).

Table 2. Values for Reference Model[a]

Variable	Value	Units
Top edge of heat source	0.0	km
Bottom edge of heat source	15.0	km
Heat generation, top edge	0	kJ m^{-2}
Heat generation, depth increase[b]	734	kJ m^{-2} km^{-1}
Asperity length	170	km
Duration	5	Myr
Thermal diffusivity	1.3×10^{-6}	m^2 s^{-1}
Heat capacity	800	J (kg K)$^{-1}$)
Density	2750	kg m^{-3}

[a]To calculate the rate of heat generation, we assume a linear increase of shear stress with depth. We use a strong fault with a coefficient of friction (μ_{app}) of 0.8 and 90% of earthquake/slip energy converted into heat. This is an extreme case.
[b]Determination method: $= \tau * v_{slip}$ and = 21.6 MPa km^{-1} × 3.4 cm yr^{-1}.

[16] In addition to the lower heat flow at asperity tips, the midpoint heat flow can be much lower than it is for infinitely long faults. For asperities 2–3 times longer than the depth extent of heat generation, heat flow at the asperity midpoint is indistinguishable from heat flow from an infinitely long fault (Figure 3). However, when the asperity length is $\leq$ the depth extent of heat generation, heat flow can be a small fraction of the magnitude for infinite faults. The example of the 170-km-long creeping section shown in Figure 2 is much longer than the inferred depth of brittle faulting in the region (~15 km).

[17] Figure 4 shows the temporal evolution of the along-strike heat flow profile for an asperity that extends to 15 km depth. Much like the case for the infinite fault of *Lachenbruch and Sass* [1980], the system evolves toward steady state, with locations closest to the fault reaching steady state sooner. The precise temporal evolution also depends on the depth extent of the heat generating fault and the thermal properties of the medium. Even though the magnitude of steady state surface heat flow at the fault tip

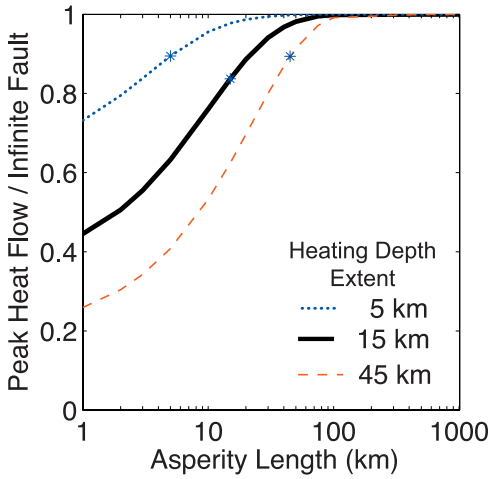

Figure 3. Peak heat flow for different lengths of heat generating asperities relative to peak heat flow for an infinitely long fault. Stars indicate the position along each curve where the asperity length is equal to the depth extent of heat generation, for reference. Heat flow is similar to infinite fault for asperities twice as long as the depth extent of heating.

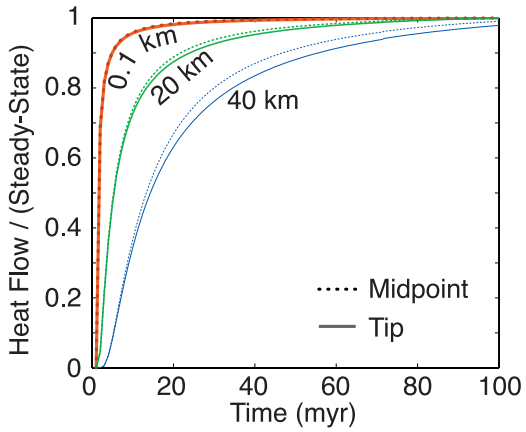

Figure 4. Temporal evolution of heat flow from a finite 170-km-long, 15-km-high asperity shown normalized by steady state values (as in Figure 2a). Distances indicate distance away from the fault along the fault perpendicular profile. Sites far from the fault do not reach steady state for tens of millions of years. Solid lines are for fault midpoint (Figure 2b). Dotted lines are for fault tips (Figure 2c). There is little difference between the temporal evolution at the tip and midpoint.

is about half the peak at the fault midpoint, the shape of the temporal evolution is very similar. Note that for the maximum age of the San Andreas fault system of ~28 Ma [*Atwater and Stock*, 1998], points 40 km from the fault only reach about 70% of their steady state value, though the heat flow at these distances is always a small fraction of the peak heat flow at the fault plane. The inferred age of the fault system in the creeping section (near Parkfield) is ~5 Ma [*Sims*, 1993], suggesting that even sites close to the fault may not have reached steady state yet.

3. Lateral Transport

[18] The models of frictional heat transport that we have discussed thus far neglect a key component of faulting: fault offset. As a fault slips, it not only displaces the geologic units in the crustal blocks surrounding it, but it also transports all of the thermal energy contained within the blocks. If the fault slip rate is fast compared to the rate of conduction, then this effect could be important. For a fault with frictional asperities, block offset can move hot material away from a heat generating asperity and juxtapose hot areas with an area that has not experienced heat generation. When these two surfaces are in contact, the direction of the thermal gradient near the fault changes direction such that flow is directed from the hot block into the cold block across the fault (instead of radially away from the fault). An analogous effect occurs for mid-ocean ridge transform fault systems [e.g., *Forsyth and Wilson*, 1984]. This effect can substantially alter the spatial and temporal distribution of heat flow. Here we include heat transport by block offset and discuss the distribution of surface heat flow for a fault with heterogeneous friction.

3.1. Method

[19] To model vertical heat flow in a system where crustal blocks and heat sources move laterally, we solve a fully coupled thermal displacement system in three dimensions. The problem cannot be solved analytically, so we use the commercially available ABAQUS finite element package using over 50,000 thermal brick elements in each model run. Because the focus of our study is on the distribution of surface heat flow, we simplify the calculation by not treating frictional stress and frictional heat explicitly. Instead, we simulate frictional heat by applying a heat flux along the asperity surface proportional to the amount of frictional work (parameters of Table 2). We impose fault slip by a simple displacement boundary condition.

3.2. A Single Asperity

[20] In Figure 5 (also Animation 1 in the auxiliary material), we show the distribution of heat flow after 5 Myr for a single frictional asperity 170 km long on a fault with block offset. As above, heat generation increases

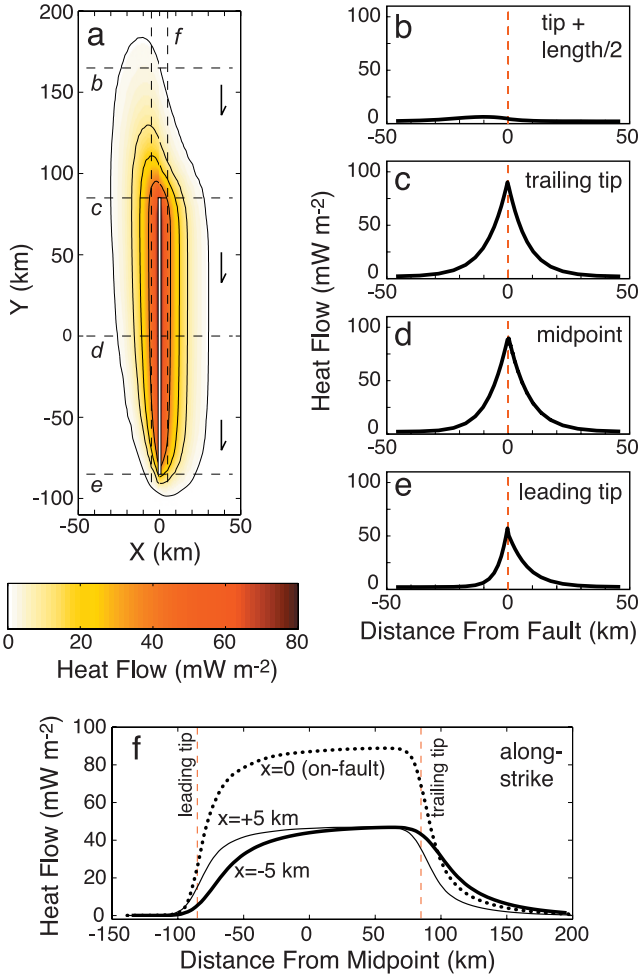

Figure 5. Heat flow distribution for a single heat-generating asperity in a model that includes block offset after 5 Myr slip at 3.4 cm yr^{-1}. Asperity is fixed to the east (right) block and has been offset 170 km. (a) Map view of surface heat flow. Heat generating surface is shown by white rectangle from $y = -85$ to $+85$ along $x = 0$. (b)–(e) Profiles perpendicular to the asperity at $y = 170$, 85, 0, -85, respectively. (f) Profile along strike of the asperity, looking west.

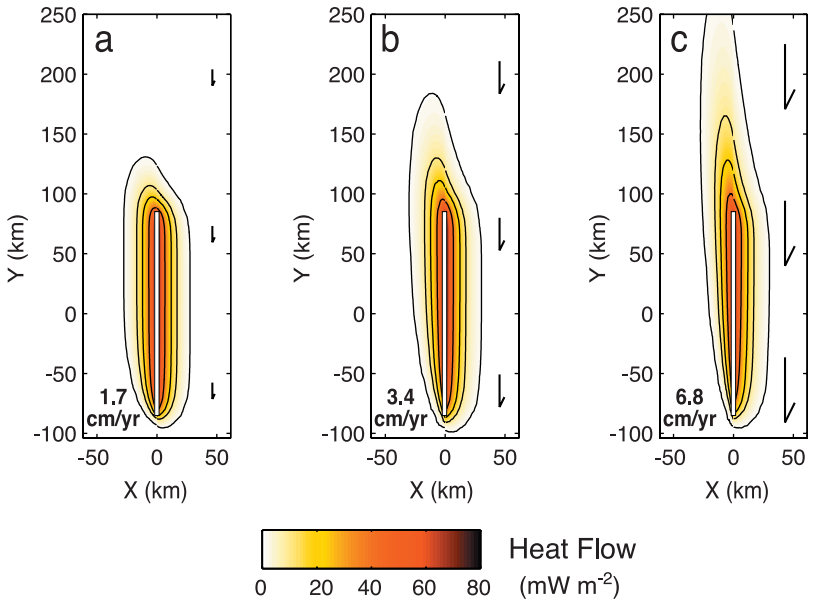

Figure 6. Surface heat flow distribution for a single frictional heat generating asperity in models that include different rates of block offset: (a) 1.7 cm yr^{-1}; (b) 3.4 cm yr^{-1}, representative of the SAF since 5 Ma [*Sims*, 1993]; and (c) 6.8 cm yr^{-1}. A solid line marks the location of the heat generating surface (-85 km $< y <$ 85 km), which is fixed to the moving eastern block as it travels past the stationary western block in a right-lateral sense. Slower slip rates are most similar to a stationary asperity (Figure 2) and faster slip rates cause greater asymmetry and a lower peak heat flow.

linearly with depth and is restricted to the upper 15 km. Here, the asperity is fixed to the eastern block which moves past the stationary western block at 3.4 cm yr^{-1} in a right-lateral sense (long-term offset rate of the SAF). We discuss alternate transport scenarios in section 4. Initially, the results are indistinguishable from an asperity in a stationary half-space. As time passes, fault offset becomes important. We focus first on the thermal history of the western block. Cooler material on the "leading edge" (southwest of asperity) is now juxtaposed with the heat source. At the trailing edge of the heat source (northwest), material that was heated progressively moves away from that heat and comes in contact with cooler material across the fault. Without additional heat input in this region, the only control on heat flow is the thermal gradient which draws heat exclusively from the recently heated west side to the cooler east side. The reference frame of the eastern block is slightly different. Since the heat source in this example is fixed to the eastern block, the crust adjacent to the frictional asperity is always heated. While the leading edge (southeast of asperity) is constantly juxtaposed with unheated western rocks, by the time these sections of the western block reach the trailing edge (north end), they have been heated for the entire time it takes to travel the length of the asperity. As a result, heat flow is most similar to the stationary case near the trailing edge because the duration of heating on both sides is similar to the case where the two sides were always in contact.

[21] The resulting heat flow distribution is asymmetric along strike (compare Figures 5b–5e) and on opposite sides of the fault (Figure 5f). The peak heat flow occurs near the northern end of the asperity (y = 75) where the heat flow pattern is most symmetric across the fault. Even though the heating rate is identical to the stationary reference case, the heat flow at the midpoint of the moving asperity is 8% lower than for a stationary case and is uniformly lower throughout the model because heat is spread over a larger area when the blocks move.

3.3. Dependence on Slip Rate

[22] The stationary fault represents one end-member of heating along a finite fault length that produces a symmetric profile, and asymmetry will arise for any nonzero fault offset rate. Because the asymmetry arises from both advective transport of the heat within blocks and the rapid juxtaposition of cooler (unheated) material with hotter sections, the precise distribution of heat flow about a finite frictional asperity depends strongly on the slip rate of the fault.

[23] Figure 6 shows the map view heat flow distribution for variations on the reference case with a range of fault displacements. To isolate the effects of displacement rate, we impose the same total heat generation in the models shown in Figure 6 (in the real world, heat generation would vary with slip rate). Because the same total heat is distributed over a larger area in the faster displacement rate cases, heat flow magnitudes are lower. For the fast case (6.8 cm yr^{-1}), the peak and midpoint heat flow are 13% and 24% lower than for the stationary fault, respectively. Changes of this magnitude would have a noticeable impact on heat flow data for natural faults.

3.4. Multiple Asperities and the Infinitesimal Limit

[24] In reality, there may be a suite of frictional asperities across a range of scales [*Brune and Thatcher*, 2002]. The ability to resolve these asperities depends on their size and the spatial resolution of observations. We calculate the heat flow distribution for three scenarios with different numbers

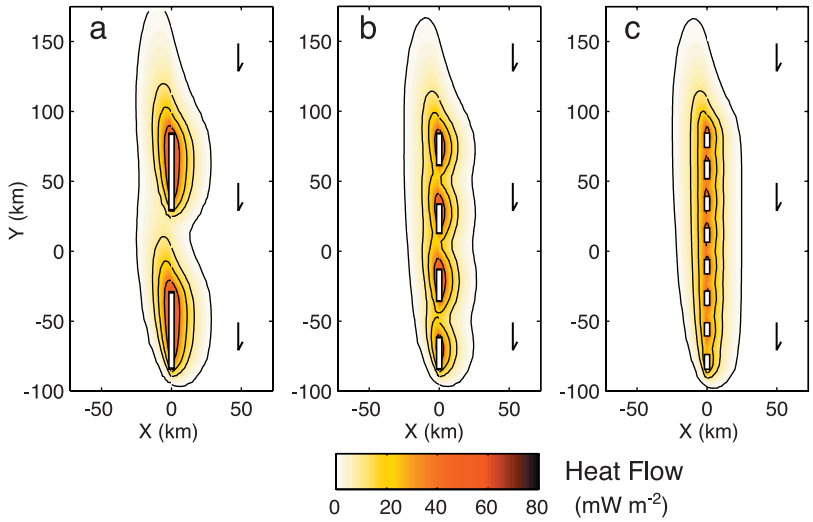

Figure 7. Surface heat flow distribution for multiple frictional heat generating asperities in models that include block offset. (a) Two 57-km-long asperities separated by 57 km; (b) four 24-km-long asperities separated by 24 km each; and (c) eight 11-km-long asperities separated by 11 km each.

of asperities (Figure 7). Each model has the same slip rate, same shear stress resisting slip, and similar total area of high-friction asperities (50–66% of the total along-strike distance of 170 km, identical 15 km depth extent of heating). The spatial pattern of heat flow along the fault plane itself is quite complex and differs dramatically among the three different examples, but at about 20 km away from the fault plane, the distributions are nearly identical. For asperities with gaps comparable to the average asperity length, heat flow becomes indistinguishable from a homogeneous fault at distances of 1–2 times the depth extent of faulting for typical thermal properties.

[25] In the early time steps of model runs with multiple asperities, the individual heat generating patches produce miniature versions of a single isolated asperity, each one slightly asymmetric in the same pattern as Figure 5a. Because these asperities are smaller and spaced close together, a section of fault that was "left behind" by the trailing edge of one asperity quickly encounters the leading edge of another asperity. If the asperities are closer together than the depth extent of faulting, then even when a section of crust is not in direct contact with a heat generating asperity, it will still be close enough for a substantial amount of heat to conduct to it from the nearby heating patches. Shorter distances between asperities also reduce the amount of time for sections of the fault to cool between being in contact with heat generating asperities. As the spacing between asperities gets smaller, we approach the limiting case of an infinite, homogeneous fault, much like integrating a series of closely spaced point sources of heat to represent a continuous heat source. Heterogeneity on natural faults will have the strongest effect on heat flow when their asperities are large compared to the depth extent of heat generation.

3.5. Asperities and Interpretations of Heat Flow

[26] The three scenarios pictured in Figure 7 all have less total heat generation than the single asperity case because they span the same distance along strike of the fault (170 km) but include frictionless gaps. Models of infinite, homogeneous faults assume that the entire surface area of a fault is generating heat, when in fact much of the heat could be generated on a few high-friction asperities. As section 3.4 demonstrates, the heat flow pattern from these two cases could be indistinguishable at reasonable distances from the fault, and we could only constrain the heat generation integrated over the entire fault area. The ratio of the area of strong asperities to the total area of the fault surface is another factor that can be lumped into the "apparent" coefficient of friction inferred when assuming homogeneous fault heating models, but one must consider this factor when interpreting μ_{app} in terms of frictional properties during sliding. Faults with bulk μ_{app} at intermediate values can result from either uniform intermediate frictional strength or pockets of strong asperities embedded in a weaker fault (e.g., $\mu_{uniform} = 0.2$ over the entire fault versus four times as high on one quarter the fault surface with the rest frictionless, $\mu_{asperity} = 0.8$), scenarios explained by very different physical mechanisms. This added complexity about interpreting constraints on μ_{app} that come from heterogeneous faults is probably the most important and generally applicable observation we can make from our modeling.

4. Is the Creeping Section Strong?

[27] Having built up a framework for evaluating heat flow near frictional asperities, we focus on the original question of the creeping section as a frictional asperity. If bodies with unique lithology control fault creep, the creeping section of the fault will have migrated over time because lithologic units are displaced as the fault accumulates offset. Figure 8 shows two possibilities for how the creeping section may have migrated over time, "displacement" and "dragging." In the displacement model (Figure 8a), the creeping segment has always been the same length, but is displaced as the fault slips. Our models from section 3 are examples of this scenario. In the dragging model (Figure 8b), the creeping section is related to a localized lithologic unit when faulting initiates, but that material is dragged along within the fault zone causing the creeping segment to grow

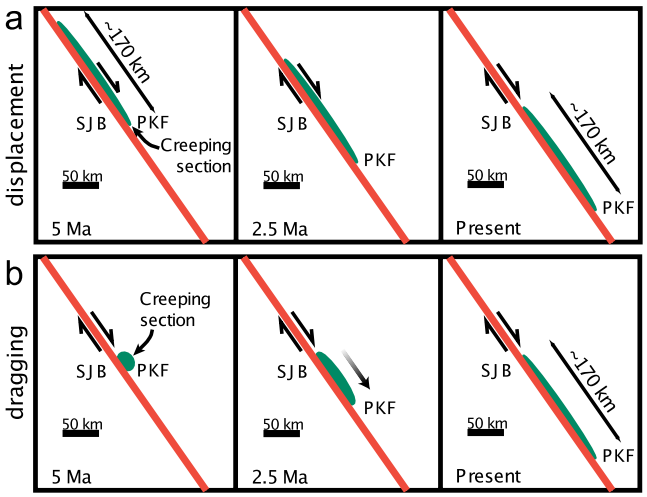

Figure 8. Two of many possible scenarios for how the length and position of the creeping section have evolved over time. (a) Displacement model. Creeping section has always been 170 km long but is displaced over time. (b) Dragging model. Material that causes creep behavior starts off as a small localized feature but is dragged along in the fault zone; creeping section grows longer over time. We show the southern end of the creeping section fixed to the northeast block because Franciscan rocks seem more likely to be the source of unique creeping behavior. Rotate heat flow patterns 180° for the opposite case.

with time (Animation 2). The active trace of the SAF in central California initiated about 4–6 Ma (with slip prior to this time dominantly occurring on abandoned traces such as the Red Hills–San Juan, Gold Hill, and Jack Ranch faults, and the San Gregorio–Hosgri system) and has accumulated approximately 160 km of cumulative offset [*Sims*, 1993].The striking coincidence between the length of the creeping section and the total amount of cumulative offset (~160 km) supports the idea that the creep may be related to a dragged lithologic unit. Other than this coincidence, we currently have no way of determining when aseismic creep initiated on the present-day creeping section and for how long it has persisted. As we show in Figure 4, asperities that exist for shorter times than the asperities illustrated in Figure 8 will produce lower magnitude heat flow anomalies. For the purposes of exploring an end-member model, we will assume that the creeping section initiated its unique creeping behavior at 5 Ma, and our conclusions are only applicable if this assumption is correct.

4.1. Models of the Creeping Section

[28] To introduce the general features of several model variations, we illustrate the spatial distribution of frictional heat anomalies for four general models in Figures 9 and 10. We define the apparent coefficient of friction for the creeping section as μ_c and the surrounding sections of the fault to the north and south as μ_s (μ_{app} will continue to be used for general statements that apply to whichever section has frictional heat generation). We consider two end-member cases of frictional heterogeneity): (1) the creeping section is frictionless ($\mu_c = 0$) while the fault further north and south is stronger ($\mu_s = 0.2$) and (2) the opposite scenario where the creeping section is relatively strong ($\mu_c = 0.2$) and the surrounding fault is frictionless ($\mu_s = 0$). A weak creeping section would correspond to a lithologic or structural feature of the creeping section that is persistently weaker than the surrounding fault, while a relatively strong creeping section could be explained physically if dynamic processes weaken the fault to the north and south while the aseismic creeping section remains unaffected by dynamic weakening. The asperity dimensions evolve over time as in the two scenarios of Figure 8. We illustrate the case where the conditions that permit creep are fixed to the North American plate as it travels southeastward (e.g., if Franciscan units northeast of the SAF drive creep behavior). For the alternate case, simply rotate the model solution 180°. We choose a constant background heat flow (76 mW m^{-2} from Uniform HF, see below) and μ_c or μ_s of 0.2 to highlight the general features of these models and facilitate qualitative comparison with observations (higher μ_{app} do not agree well with the data). See section 4.2 for a quantitative comparison and best fitting values of these parameters.

[29] All models result in an asymmetric distribution of heat flow across the fault. For an observer standing at the midpoint of a strong frictional asperity with a right-lateral sense of slip, the highest heat flow will always be on his or her left side when looking in either direction along strike. Along strike (Figure 10), the displacement models have the most extreme values and cover the broadest area at the trailing edge of the asperity (north end when heat source fixed to east side of right-lateral fault running north-south). The distribution from the dragging model (Figures 9c–9d) is asymmetric from one side of the fault to the other, but would look identical when rotated by 180°. Dragging from north to south is therefore identical to the opposite case, so a snapshot in time of heat flow would not allow us to determine where the dragged unit originated.

4.2. Quantitative Comparison of Data and Models

[30] In sections 4.2.1–4.2.3, we compare existing surface heat flow observations to various model scenarios. Our goal is to determine the value of μ_c and μ_s most consistent with the data, as well as the maximum coefficients of friction allowed by the data.

4.2.1. Background Heat Flow

[31] Our numerical model results provide the spatial distribution of frictional heat anomalies, or contributions of heat flow above a background value. A rigorous statistical comparison of model results with observations requires quantifying the details of background heat flow.

[32] Heat flow measurements far from the fault are unaffected by frictional heating and therefore should serve as reliable measures of background heat flow. Even though our study area is restricted to the central Coast Ranges, measurements >30 km from the active SAF show considerable scatter, ranging from 60 to 96 mW m^{-2} with limited spatial coherence. Models that assume existing heat flow data represent random scatter about a uniform background heat flow with no frictional heat (Uniform HF) do not, on average, fit the data within their 95% confidence limits (χ^2/DOF of 4.7; Table 3; confidence values determined by looking up χ^2/DOF in a χ^2 cumulative distribution table for one degree of freedom). Including frictional heat on top of a

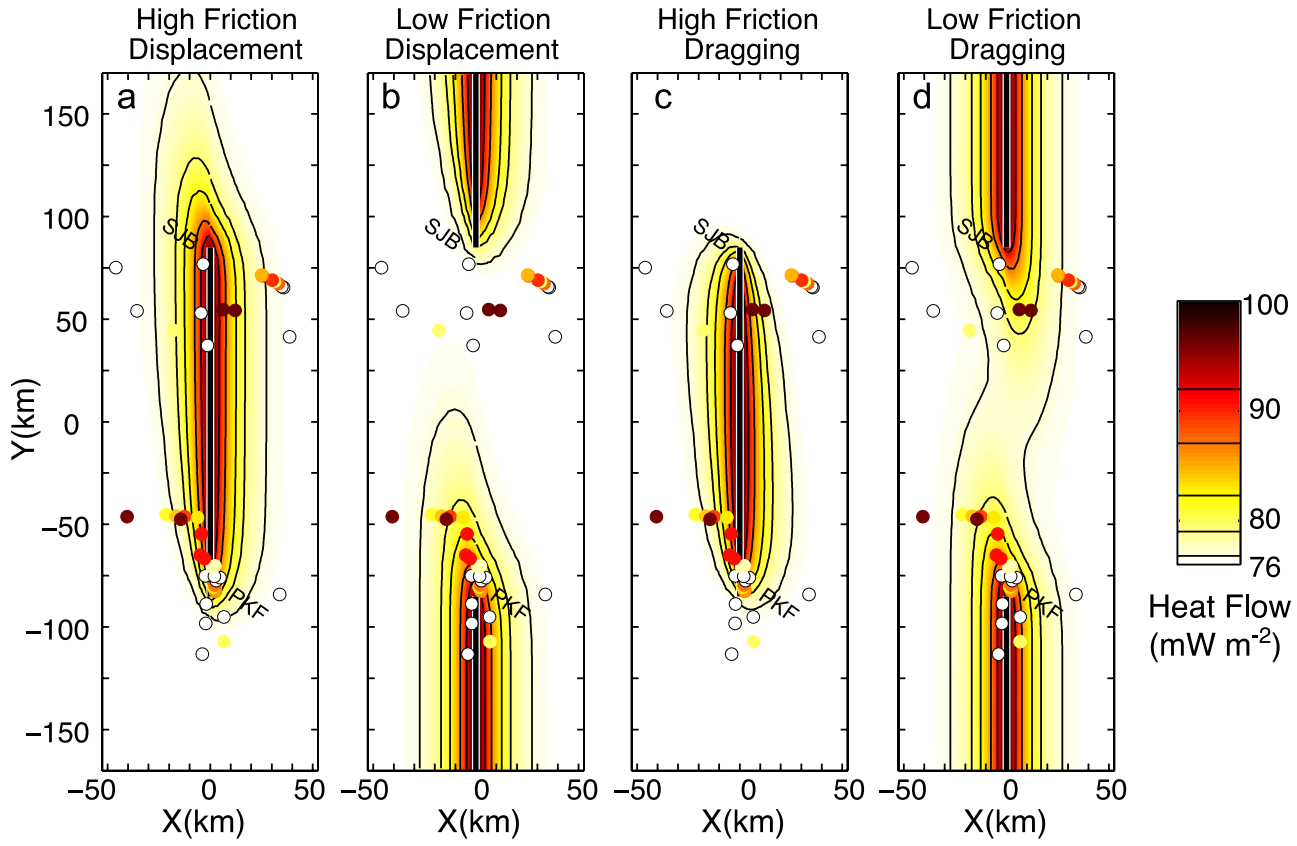

Figure 9. Predicted heat flow for the model creeping section after 5 Myr of fault activity (assuming 76 mW m^{-2} uniform background heat flow and $\mu_{app} = 0.2$ on either creeping or surrounding SAF segments). Sections of fault along $x = 0$ are either strong (thick bar) or weak. Creeping section ($-85 < y < 85$) has coefficient of friction μ_c; surrounding fault, μ_s. (a) Displacement geometry with stronger creeping section ($\mu_c = 0.2$, $\mu_s = 0$). (b) Displacement geometry with weak creeping section ($\mu_c = 0.$, $\mu_s = 0.2$). (c) Dragging geometry with stronger creeping section ($\mu_c = 0.2$, $\mu_s = 0$). (d) Dragging geometry with weak creeping section ($\mu_c = 0$, $\mu_s = 0.2$). Dots indicate heat flow observations from Figure 1. Color scale is saturated so white heat flow dots are below assumed background heat flow. Data are shown for qualitative comparison only, as the background heat flow likely varies from the uniform value assumed for this figure (see Figure 11). Coefficient of friction of 0.2 is arbitrarily chosen for illustration; see Table 3 for best fitting value. Horizontal lines on color bar show contour values, irregularly spaced to emphasize shape. SJB, San Juan Bautista; PKF, Parkfield.

uniform background heat flow (section 4.2.2) fits the data slightly better, but still not within 95% confidence (χ^2/DOF of 4.6, uniform+μ_c).

[33] Several models predict systematic variations in what we refer to as background heat flow that we should incorporate. *Lachenbruch and Sass* [1980] show that background heat flow throughout the Coast Ranges is higher than the surrounding areas and not uniform. This "Coast Ranges high" is much broader than the anomalies we predict for frictional heat in the brittle upper crust and has been attributed to deep viscous heating [e.g., *Thatcher and England*, 1998] or hot asthenospheric intrusion into a "slab window" as the Farallon plate disappears from beneath California as the Mendocino triple junction moves northward [e.g., *Lachenbruch and Sass*, 1980; *ten Brink et al.*, 1999; *Guzofski and Furlong*, 2002]. The stalled Monterey microplate underlying portions of our study area may further modify the background heat flow [*ten Brink et al.*, 1999]. The exact magnitude of background heat flow variation from these processes depends on model parameters and assumptions that are outside the scope of this investigation, but the models have the same general features of heat flow declining with distance south of the Mendocino triple junction and lower heat flow in the Great Valley than the Coast Ranges. Figure S1 illustrates a 2-D distribution of background heat flow determined by merging two 1-D models. In those models, heat flow declines about 1 mW m^{-2} for every 20 km traveled southeast along the Coast Ranges [after *Guzofski and Furlong*, 2002], and heat flow drops by 30 mW m^{-2} over a ~100-km-wide transition across the eastern edge of the Coast Ranges [*Lachenbruch and Sass*, 1973; *Williams et al.*, 2004]. For the most part, models constrain the along-strike variation in the North American plate better than the east-west variation. While the heat flow measurements near the creeping section do fit some aspects of this scenario (especially the heat flow gradient near Parkfield), the observations are not consistent in detail. Most notably, heat flow west of the SAF near Monterey is lower than heat flow in the Great Valley east of San Juan Bautista. We have explored variations on

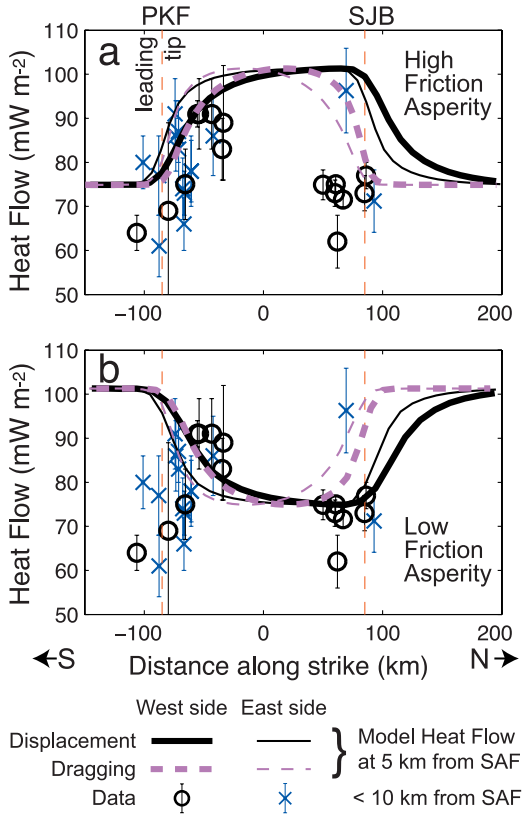

Figure 10. Profiles along the models of Figure 9 as a function of distance along fault strike. Thick lines are for a profile parallel to fault and 5 km east; thin lines are for 5 km west. Data shown are within 5 km of the fault on each side. Solid lines for a creeping section that evolves by displacement; dashed for dragging. Results (a) for a frictionally strong creeping section surrounded by frictionless fault sections to the north and south and (b) for a weak creeping section. Models have uniform background heat flow of 76 mW m^{-2} and μ_{app} of 0.2.

Figure S1 including changing the magnitude of the anomaly and shifting it in space to account for uncertainty in its location. We also tested models that include frictional heat and spatially varying background heat flow like Figure S1 (model CR+μ_c). Many of these models require negative coefficients of friction (physically meaningless, or the unlikely possibility that the fault is a localized heat sink in this region due to, for example, endothermic mineralization reactions) to fit the data, and the misfit is larger than the simpler Uniform HF model. No model where we assume background heat flow from the Coast Ranges high (with or without frictional heat) explains the spatial variation in heat flow data near San Juan Bautista. We therefore cannot use this class of simple models to assume a known background heat flow distribution for our study area.

[34] We defer to an ad hoc method of removing the background heat flow signature in order to accomplish our goal of constraining the magnitude of frictional heat above the background. We divide the area into five subregions (Figure 1) with spatially coherent heat flow and solve for independent background heat flow in each. Because the SAF appears to be a dominant heat flow boundary near San Juan Bautista, we restrict each subregion to a single side of the fault (except the central subregion, PKN-W where only 1 observation exists east of the fault). This method assumes background heat flow is roughly constant over the spatial scale of each subregion (<50 km). While this may not be strictly true, this scale is similar to or smaller than the observed heat flow transition on the edge of the Coast Ranges high [*Williams et al.*, 2004]. Solving for the best fitting background heat flow in these five subregions with no frictional heat (Table 3, subregion HF) fits the data, on average, within their 92% confidence region; the χ^2/DOF is 3.1. Estimates of background heat flow are 64–93 mW m^{-2} for different models and subregions. Adding additional subregions does not produce a statistically significant improvement to model fit, according to an *f* ratio test for adding additional model parameters. We explore moving the subregion boundaries near Parkfield and find that the changes do not substantially alter our constraints on the coefficient of friction. While not ideal, this technique for estimating best fitting background heat flows allows us to focus on our goal of constraining the magnitude of frictional heating.

4.2.2. Best Fit Coefficient of Friction

[35] We use an iterative least squares algorithm to find the parameters that best match observed heat flow. As described in section 4.1, we evaluate end-member cases where one part of the fault is assumed to be frictionless. For each model scenario, we simultaneously solve for (1) a uniform frictional strength for the entire asperity (μ_c for scenarios where we assume $\mu_s = 0$ and μ_s where $\mu_c = 0$); (2) background heat flow for each subregion; and (3) location of the asperity along strike. We solve for this location because the "endpoints" of the creeping section are not well defined. We allow the asperity to shift up to 20 km in either direction along strike from our preferred position of the creeping section ($Y_{shift} = 0$, inferred from changes in surface creep rates compiled by *Titus et al.* [2005], thick grey line of Figure 1).

[36] The best fitting coefficient of friction for all scenarios is <0.1, indicative of a weak fault (Table 3). Different models result in lower misfit in different subregions. For example, the models differ most in their ability to fit data west of the fault near San Juan Bautista (SJB-W). Almost no model is able to improve the misfit east of the fault near San Juan Bautista (subregion SJB-E) over the Subregions HF model. This is because heat flow far from the fault is highly scattered (boreholes indicated by codes PT0 to PT9). The best fitting overall model with a χ^2/DOF slightly less than 2.7 (Displacement, 100-km-long creeping section fixed to northeast side with a $\mu_c = 0.10 \pm 0.02$ and $\mu_s = 0$) has a 13% lower χ^2 misfit than the Subregion HF model that excludes frictional heat. Similar misfit exists for other models. An *f* ratio test shows that estimation of the additional model parameter is statistically worthwhile at the 98% confidence level, meaning frictional heat is statistically preferred over simpler models. A coefficient of friction ~0.1 is therefore preferred over a frictionless fault or higher strength fault.

4.2.3. Is a Strong Fault Consistent With the Heat Flow Observations?

[37] While the best fitting parameters for all models indicate a low μ_c or μ_s, do any of the scenarios allow for a strong asperity? We constrain the coefficients of friction to 0.2, 0.4, and 0.8 and then solve for the best fitting asperity

Table 3. Best Fitting Model Parameters and Misfit Statistics[a]

Model					χ^2/DOF Subregion					Best Fit Heat Flow, mW m^2						
					SJB		PKN	PKS		SJB		PKN	PKS			
Name	Length, km	NE/SW	Y_{shift}, km	χ^2/DOF Total	W	E	W	W	E	W	E	W	W	E	$\mu_s \pm 1\sigma$	$\mu_c \pm 1\sigma$
Background Heat Flow Only																
Uniform HF	–	–	–	4.7	6.2	3.3	7.2	7.4	1.5	76 ± 1[b]	76 ± 1[b]	76 ± 1[b]	76 ± 1[b]	76 ± 1[b]	0.00[c]	0.00[c]
CR high	–	–	–	5.2	3.8	4.9	7.6	7.2	3.4	[d]	[d]	[d]	[d]	[d]	0.00[c]	0.00[c]
Subregion HF	–	–	–	3.1	3.6	3.2	0.8	6.6	1.5	72 ± 1	79 ± 2	90 ± 2	81 ± 2	76 ± 2	0.00[c]	0.00[c]
Best Fit Parameters																
Uniform+μ_c	170	NE	20	4.6	6.8	3.2	5.8	6.9	1.6	78 ± 1[b]	78 ± 1[b]	78 ± 1[b]	78 ± 1[b]	78 ± 1[b]	0.00[c]	−0.04 ± 0.01
CR+μ_c	170	NE	5	5.1	3.8	4.9	7.5	7.2	3.4	Figure S1 + 13 ± 1	Figure S1 + 13 ± 1	Figure S1 + 13 ± 1	Figure S1 + 13 ± 1		0.00[c]	0.01 ± 0.01
Displacement	170	NE	−14	2.7	1.7	3.3	1.1	7	1.2	65 ± 2	78 ± 2	87 ± 2	80 ± 2	71 ± 2	0.00[c]	0.07 ± 0.02
Displacement	170	SW	19	2.8	1.8	3.3	1.1	6.9	1.4	66 ± 2	78 ± 2	87 ± 2	80 ± 2	73 ± 2	0.00[c]	0.07 ± 0.02
Displacement	170	NE	−17	2.9	3.7	3.1	0.9	2.4	2.2	72 ± 1	79 ± 2	93 ± 2	85 ± 3	81 ± 2	−0.17 ± 0.05	0.00[c]
Displacement	170	SW	−20	3.0	2.8	3.3	0.8	7.3	1.5	70 ± 1	78 ± 2	90 ± 2	80 ± 2	76 ± 2	0.06 ± 0.03	0.00[c]
Displacement	100	NE	9	2.7	1.7	3.1	0.8	6.6	1.5	64 ± 2	78 ± 2	90 ± 2	81 ± 2	76 ± 2	0.00[c]	0.10 ± 0.02
Displacement	100	SW	20	2.8	2.0	3.2	0.9	6.7	1.5	65 ± 2	78 ± 2	89 ± 2	81 ± 2	75 ± 2	0.00[c]	0.09 ± 0.02
Dragging	170	NE/SW	−6	2.7	1.8	3.3	1.1	6.8	1.2	66 ± 2	78 ± 2	87 ± 2	80 ± 2	71 ± 2	0.00[c]	0.08 ± 0.02
Dragging	170	NE/SW	−20	3.1	3.2	3.2	0.8	7.2	1.5	71 ± 1	79 ± 2	90 ± 2	80 ± 2	75 ± 2	0.02 ± 0.03	0.00[c]
Dragging	100	NE/SW	20	2.7	1.9	3.2	0.8	6.6	1.5	65 ± 2	78 ± 2	90 ± 2	81 ± 2	76 ± 2	0.00[c]	0.09 ± 0.02
Calaveras	–	–	−13	2.7	1.7	3.3	1.1	7.1	1.2	66 ± 2	78 ± 2	87 ± 2	80 ± 2	71 ± 2	0.00[c]	0.07 ± 0.02
Assume μ_{app} = 0.2, Estimate Best Fit Heat Flow																
Displacement	170	NE	20	3.5	3.5	4.5	1.4	6.6	1.5	55 ± 1	76 ± 2	88 ± 2	81 ± 2	75 ± 2	0.00[c]	0.20[c]
Displacement	170	SW	20	3.8	3.3	4.4	2.7	7.7	1.7	55 ± 1	77 ± 2	81 ± 2	80 ± 2	67 ± 2	0.00[c]	0.20[c]
Displacement	170	NE	−19	3.9	3.3	3.3	1.0	14.7	1.3	71 ± 1	78 ± 2	87 ± 2	76 ± 2	70 ± 2	0.20[c]	0.00[c]
Displacement	170	SW	−18	3.4	2.6	4.2	0.8	9.3	1.5	66 ± 1	76 ± 2	90 ± 2	79 ± 2	75 ± 2	0.20[c]	0.00[c]
Displacement	100	NE	9	3.1	3.7	3.2	0.9	6.6	1.5	56 ± 1	77 ± 2	90 ± 2	81 ± 2	76 ± 2	0.00[c]	0.20[c]
Displacement	100	SW	18	3.1	3.6	3.1	1.1	6.8	1.5	58 ± 1	78 ± 2	88 ± 2	80 ± 2	73 ± 2	0.00[c]	0.20[c]
Dragging	170	NE/SW	14	3.5	3.5	4.3	1.5	6.6	1.5	55 ± 1	77 ± 2	87 ± 2	81 ± 2	75 ± 2	0.00[c]	0.20[c]
Dragging	170	NE/SW	−4	3.8	2.5	3.2	1.3	15.3	0.9	69 ± 1	78 ± 2	85 ± 2	75 ± 2	64 ± 2	0.20[c]	0.00[c]
Dragging	100	NE/SW	20	3.1	3.7	3.4	0.8	6.6	1.5	57 ± 1	78 ± 2	90 ± 2	81 ± 2	76 ± 2	0.00[c]	0.20[c]
Calaveras	–	–	20	3.2	2.5	4	1.9	6.7	1.5	57 ± 1	76 ± 2	86 ± 2	81 ± 2	75 ± 2	0.00[c]	0.20[c]
Assume μ_{app} = 0.4, Estimate Best Fit Heat Flow																
Displacement	170	NE	20	8.6	19.9	8.4	2.6	6.6	1.6	38 ± 1	73 ± 2	85 ± 2	81 ± 2	74 ± 2	0.00[c]	0.40[c]
Displacement	170	SW	20	9.6	18.2	7.5	7.3	9.3	2.8	39 ± 1	74 ± 2	72 ± 2	78 ± 2	58 ± 2	0.00[c]	0.40[c]
Displacement	170	NE	−19	5.5	3.2	3.5	1.4	26.2	1.7	71 ± 1	78 ± 2	84 ± 2	70 ± 2	65 ± 2	0.40[c]	0.00[c]
Displacement	170	SW	4	4.4	2.2	3.4	0.8	21.5	1.2	68 ± 1	76 ± 2	90 ± 2	73 ± 2	71 ± 2	0.40[c]	0.00[c]
Displacement	100	NE	−20	5.2	10.1	3.1	3.3	6.7	1.8	54 ± 1	78 ± 2	83 ± 2	81 ± 2	73 ± 2	0.00[c]	0.40[c]
Displacement	100	SW	−10	5.3	7.2	3.2	5.9	8.3	2.0	65 ± 1	79 ± 2	75 ± 2	79 ± 2	63 ± 2	0.00[c]	0.40[c]
Dragging	170	NE/SW	14	8.3	19.3	7.5	3.0	6.6	1.6	39 ± 1	74 ± 2	84 ± 2	81 ± 2	74 ± 2	0.00[c]	0.40[c]
Dragging	170	NE/SW	−6	5.7	2.2	3.7	2.4	27.8	1.7	67 ± 1	76 ± 2	80 ± 2	69 ± 2	54 ± 2	0.40[c]	0.00[c]
Dragging	100	NE/SW	−19	3.6	3.8	3.2	3.1	6.6	1.5	70 ± 1	79 ± 2	84 ± 2	81 ± 2	74 ± 2	0.00[c]	0.40[c]
Calaveras	–	–	20	6.9	13.7	6.6	3.9	6.7	1.5	42 ± 1	73 ± 2	82 ± 2	81 ± 2	74 ± 2	0.00[c]	0.40[c]
Assume μ_{app} = 0.8, Estimate Best Fit Heat Flow																
Dragging	100	NE/SW	−19	5.5	7.2	3.2	8.5	6.7	1.7	68 ± 1	79 ± 2	79 ± 2	81 ± 2	73 ± 2	0.00[c]	0.80[c]

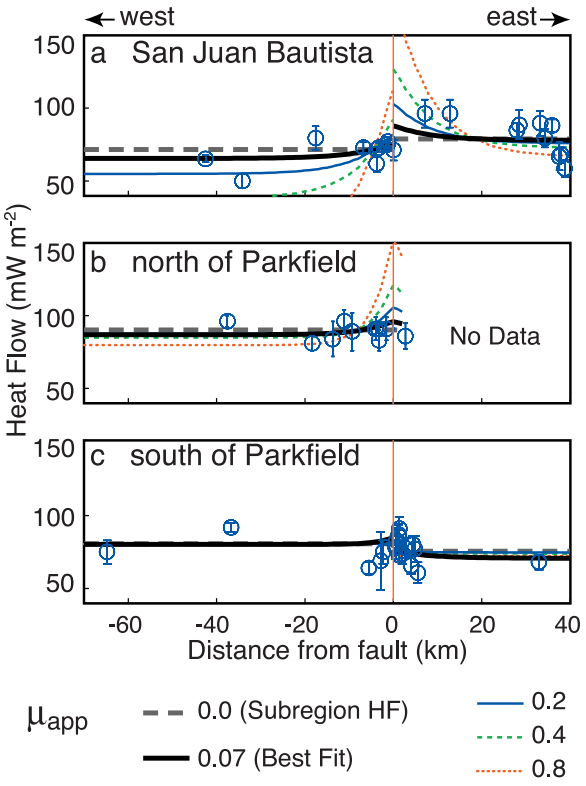

Figure 11. Heat flow along transects of representative models based on a 170-km-long high-friction asperity ($\mu_c \geq 0$, $\mu_s = 0$) with displacement time history (Figure 9a) (lines) and data (symbols). We use full 2-D distribution of heat flow to calculate model fit but illustrate only 1-D transects here. (a) Near San Juan Bautista (SJB). (b) North of Parkfield, including SAFOD and sites farther north (PKN). (c) Near Parkfield, including all sites south of SAFOD (PKS). Model transects are at midpoint along strike of each box in Figure 1. We calculate an independent background heat flow for each side of fault in each subregion but a single μ_c for the entire asperity. In Figure 11c, predicted heat flow remains relatively insensitive to different μ_c because asperities terminate north of this profile.

position and background heat flow as above (see Table 3). The data are not compatible with $\mu_c = 0.8$ or $\mu_s = 0.8$ in any model scenario at the 95% confidence level. Models where we assume this Byerlee-like frictional strength have χ^2 misfits ranging from 5.5 to 36, about 2–10 times worse than for the best fitting models. These high misfits indicate that lower μ_{app} models are much more consistent with the data. A value of $\mu_{app} = 0.4$ is also incompatible with the data in most scenarios. For the case of a 100-km-long creeping section that evolves by Dragging, the model with $\mu_c = 0.4$ and $\mu_s = 0$ barely fits the data within their 95% confidence limits, but has a χ^2 that is 18% higher than the simpler model with no frictional heating (Subregion HF). Models with $\mu_{app} = 0.2$ also fit the data within their 95% confidence limits and also have χ^2 slightly higher than the model Subregion HF.

[38] In summary, the data prefer μ_c and $\mu_s < 0.1$ on the creeping SAF and adjacent fault segments, but are statistically permissive of coefficients of friction as high as 0.2 in most cases. The gap in heat flow observations in the central creeping section allows a 100-km-long asperity with $\mu_c = 0.4$ to remain undetected only if the Dragging model is correct. Available heat flow data are not consistent with a frictional asperity having $\mu_{app} > 0.4$ for any model scenario that we considered.

4.3. Key Features of Misfit

[39] Even the best fitting models have substantial χ^2 misfit. There are three main features that prevent a better fit between data and model: (1) models produce heating localized near the fault which is not observed in the data; (2) heat flow in models is asymmetric across the fault in an opposite sense to observed heat flow; and (3) there may be complicated variations in regional background heat flow observations. We discuss each of these issues below.

[40] In models, frictional heat causes heat flow to vary systematically as a function of distance from the fault. While statistically permissive of frictional heat, the heat flow observations show no obvious near-fault anomaly and do not vary systematically as a function of distance from the fault (Figure 11) [also *Lachenbruch and Sass*, 1980, 1981]. This observation remains the most compelling argument against the hypothesis of a strong creeping section.

[41] In addition to the crucial overall lack of localized heat flow anomalies, we can compare other features of the spatial distribution in the data and models. The data show a clear decrease in heat flow from north to south along strike near Parkfield (Figure 10). Our models show a similar decrease in heat flow occurring over a similar length scale for the southern tip of the creeping section asperity. There appears to be good correspondence between the data and model of a strong creeping section for this feature, especially in data within 5 km southwest side of the fault (Figure 10). Despite the apparent visual agreement, the χ^2/DOF for the subregion as a whole (PKS-W) is still poor overall (6.6 for the best fitting high friction asperity) because observations far from the fault are high relative to the best fitting background heat flow estimates (Figure 11c).

[42] Both observations and models show distinct asymmetry across the fault, especially immediately adjacent to

Notes to Table 3:

[a]Model scenario name (see Figure 8); length, creeping section length at end of model run; H/L, high for high-friction creeping section surrounded by frictionless fault everywhere else, low for opposite case; NE/SW, NE for properties leading to fault creep travel with northeast side of fault, SW for southwest. For dragged models, the solution is identical for both cases. Calaveras fault is calculated as a stationary asperity; Y_{shift}, distance model is shifted along the y axis to produce the lowest misfit with observations. χ^2/DOF total, sum of χ^2 misfit for the entire model divided by, DOF, the number of degrees of freedom; χ^2/DOF for each of the five subregions; best fitting background heat flow and 1σ uncertainties; μ_s and μ_c best fitting coefficient of friction for creeping section and surrounding areas. Subregions are SJB, San Juan Bautista ($y > 20$); PKN, north of Parkfield ($-70 < y < -40$, includes SAFOD); PKS, southern Parkfield area ($y < -70$, south of SAFOD); E, east of SAF; W, west of SAF. All table values are dimensionless unless indicated.

[b]Uniform HF model solves for a single heat flow value that applies to all subregions.

[c]Quantity fixed to the given value rather than estimated.

[d]Models with CR are based on a spatially complex background heat flow illustrated in supplementary Figure S1. Shifting that distribution uniformly higher by 13 ± 1 mW m^{-2} provides the best fit to the data in both models. See section 4.2.1, paragraph 33.

the fault near San Juan Bautista (Figure 11a) where heat flow data span both sides. The lowest heat flow observations in the region occur west of the fault here, but models of a strong creeping section predict the opposite, the southwest side of the fault should have heat flow higher above the background than the northeast. The asymmetry in the observations is evident even in stations less than 10 km apart on opposite sides of the fault, indicating a relatively shallow mechanism affecting heat flow (potentially a hydrologic signature, but could also reflect recent differences in the exhumation history on opposite sides of the fault or differences in radiogenic heat production). If interpreted in terms of frictional heat on an asperity along a right-lateral fault, the sense of asymmetry in the observations is most consistent with a weak creeping section (Figures 9b and 9d), or, alternatively, a strong creeping section with left-lateral offset (obviously inconsistent with the SAF).

4.4. Other Factors Affecting Local Heat Flow

[43] In addition to the Coast Ranges high mentioned above, other factors can produce spatial variations in heat flow that are not considered in our modeling. Volcanism and exhumation can perturb regional heat flow. *Blythe et al.* [2004] show that at least one location near Parkfield along the San Andreas fault was relatively unaffected by such events since ~60 Ma, but Miocene volcanism related to the migration of triple junctions at the formation of the young San Andreas fault undoubtedly affected the heat flow locally throughout the Coast Ranges. In this study, we focus on frictional heat generation since 5 Ma, long after this volcanism subsided in the Parkfield area [*Sims*, 1993].

[44] Our models do not consider the contribution of nearby fault segments or any complex three-dimensional geometry of the SAF system. Frictional heat generation on closely spaced fault segments can also produce broader heat flow anomalies. *Williams et al.* [2004] show the effect of the active San Gregorio fault on heat flow profiles, but at the latitude of the creeping SAF this fault is so far away that it produces an essentially isolated heat flow anomaly. The Calaveras fault and the SAF intersect near San Juan Bautista at the northern end of Figure 1. Because the Calaveras fault is also known to creep, Figure S2 shows the expected distribution of heat flow for a frictionally strong Calaveras fault intersecting the creeping section asperity. The lower slip rate on the Calaveras fault (12–15 mm yr^{-1}) produces a heat flow anomaly that is proportionally smaller than the anomaly about the creeping section. The existing heat flow observations closest to the fault junction are tens of kilometers south of the Calaveras fault and almost entirely unaffected by a localized heating anomaly from it. Table 3 shows that the Calaveras model has statistically comparable misfit to our other models, so the inclusion of a strong Calaveras fault does not affect our conclusions.

[45] Along with complex geometry, individual traces of the fault become active and inactive over time as fault systems migrate at a range of scales. This migration will lead to broader heat flow anomalies with lower peak magnitudes. Inactive faults which may have played important roles in accommodating past plate boundary deformation, such as the Rinconada fault [*Jachens et al.*, 1998], would only make contributions to the present-day heat flow if they were active within the last few Myr. With better geologic constraints on the development and evolution of individual fault traces in the area, we can use models such as the ones presented here to simulate the spatially and temporally complex heat generation along finite faults.

5. Implications for Strength of the San Andreas Fault and Dynamic Weakening Mechanisms

[46] With existing heat flow measurements inconsistent with a strong frictional asperity along the creeping section ($\mu_{app} > 0.4$), we suggest that the creeping section is weak. The observation of a weak creeping section is in agreement with seismologically determined stress orientations with maximum compressive stress axes (S_{Hmax}) at high angles (70°–90°) to the strike of the SAF [*Provost and Houston*, 2001; *Townend and Zoback*, 2004; *Hardebeck and Michael*, 2004]. Variations in stress orientations can also give insight into variations in frictional strength along fault strike. For example, *Townend and Zoback* [2004] show that the average orientation of S_{Hmax} relative to the local SAF along a ~400 km length of the fault in Southern California is approximately 68 ± 7°. This value from the locked southern section is similar to that obtained for the deepest measurement made in the SAFOD Pilot Hole in the creeping section [69 ± 14°, *Hickman and Zoback*, 2004], but different from the corresponding angle on the locked section farther north (>80° on the San Francisco Peninsula [*Townend and Zoback*, 2004]), reflecting strength variations between these fault sections. Using a similar data set and technique, *Provost and Houston* [2001] suggest that the creeping section displays different mechanical behavior than the San Andreas fault system farther to the north [*Provost and Houston*, 2003] and south [*Hardebeck and Hauksson*, 1999] where stress axes are at lower angles (~40°–60°) near the fault, relative strength variations confirmed by *Hardebeck and Michael* [2004].

[47] Our modeling can also help constrain the strength of the creeping section relative to surrounding sections of the fault. While the sense of asymmetry in the heat flow (section 4.3) is permissive of a weak creeping section embedded along strike in a stronger fault, our modeling suggests that the magnitude of this strength contrast is small. When we explore the case of a frictionless creeping section surrounded by a stronger SAF, the best fitting model prefers $\mu_s < 0.1$ for the SAF north and south of the creeping section in our study area. This value is not reliably distinguishable from our best estimates of μ_c, so we cannot definitively determine if the creeping section is stronger than adjacent sections of the fault or vice versa. More reliable heat flow measurements would better constrain the relative strengths of creeping and noncreeping sections, allowing for a better understanding of the contribution of creeping behavior to fault strength. Our existing heat flow data loosely constrain the absolute strength of the creeping section and show its strength is qualitatively similar to the surrounding fault sections.

[48] Because the creeping section does not slip in large earthquakes, it cannot be weakened by dynamic mechanisms. Therefore persistent weaknesses related to fault zone lithology or permeability structure must be responsible for the weakness of the creeping section. Distinguishing between specific persistent weakening mechanisms requires direct observations of fault zone pore pressures, permeabil-

ity structure, and gouge materials. Some evidence does exist to suggest that serpentine minerals may weaken along the creeping section. *Irwin and Barnes* [1975] suggest that a horizontal lens of low-permeability serpentinite could block fluid migration and might lead to persistently elevated fluid pressures within the fault zone. Alternatively, a deep source of fluids beneath central California related to dehydration of serpentine minerals could cause elevated fluid pressures localized near the San Andreas fault system [*Brocher et al.*, 2003]. Serpentine could also be the source of frictionally exotic gouge, as surface mapping of the SAF in part of the creeping section north of Parkfield shows serpentinite forms the core of the fault [*Evans et al.*, 2004; *Rymer et al.*, 2004]. The SAFOD borehole, which penetrated the SAF at 3 km depth, also encountered serpentinite in close association with the fault zone at depth. While direct evidence for serpentine minerals is found along the creeping section of the SAF, they are not necessarily present along all fault zones. As such, persistent weakness related to serpentine alone may not be sufficient to explain the strength of all faults or the entire SAF system.

6. Additional Heat Flow Observations

[49] New heat flow observations from Plate Boundary Observatory (PBO) strainmeter boreholes could provide valuable measurements for constraining frictional heat anomalies. Coverage on both sides of the fault is essential to capture any asymmetry, with measurements from <10 km being most useful for quantifying localized heating. Since the seismogenic zone is about 14 km deep near Parkfield [*Murray et al.*, 2001], observations from >40 km are considered "background" values (which are essential, but can be sparse). The ideal maximum spacing between stations along strike would be ~14–28 km, or 1–2 times the depth extent of heat generation. The proposed PBO installations will leave gaps >75 km in the central creeping section of the SAF. Because of this gap, we still will not be able to rule out the existence of a strong frictional asperity 100 km long (or shorter) near the center of the creeping section.

7. Conclusions

[50] Localized high-friction asperities will produce localized heating. If these asperities are tied to the crustal block on one side of the fault, they will migrate over time producing a strongly asymmetric heat flow pattern whose magnitude is smaller than that of a stationary asperity. This effect is a strong function of slip rate, asperity size, and the temporal history of the heat source. The asymmetry is most pronounced near the leading edges and beyond the trailing edges of the heat sources. A single profile across a fault would therefore not capture the full complexity of the heat flow signal, nor would the peak heat flow be as large as has been predicted by models of infinitely long, uniform faults. Recognizing zones of heterogeneous high friction is best accomplished with a dense distribution of stations within 1–2 times the depth extent of the heat source. Heat flow near the San Andreas fault shows heat flow patterns that are asymmetric across the fault and along strike. This asymmetry, however, is opposite that predicted for a strong frictional asperity along the creeping section even when differing background heat flows are subtracted from both sides. Further, heat flow does not vary systematically as a function of distance from the fault. If our assumption that the creeping section has been actively creeping since 5 Ma is correct, existing heat flow data in the area provide enough spatial coverage to rule out the possibility of an exceptionally strong creeping section ($\mu_{app} = 0.8$) embedded along strike in a weaker fault. For all our model scenarios, $\mu_{app} \leq 0.1$ on both the creeping SAF and adjacent fault segments is most consistent with the data. Because the creeping section does not slip in large earthquakes, the mechanism controlling its weakness is not related to dynamic processes resulting from high slip rate earthquake ruptures. At least for the weak creeping section, this lack of heat flow anomaly in central California would rule out thermal pressurization of fault zone fluids, acoustic fluidization, wrinkle-like slip pulses, and other dynamic processes as the mechanisms that control frictional strength.

[51] **Acknowledgments.** This work conducted thanks to generous funding from a National Science Foundation Graduate Research Fellowship, NSF-EarthScope grant EAR-0346188, and a U.S. Geological Survey Mendenhall Postdoctoral Fellowship. We acknowledge and thank Jim Brune for encouraging us to test his thought provoking hypothesis, as well as his supportive reviews of the manuscript. J. Andrews, P. Fulton, D. Moore, and J. Townend all provided valuable comments on the manuscript.

References

Andrews, D. J. (2002), A fault constitutive relation accounting for thermal pressurization of pore fluid, *J. Geophys. Res.*, *107*(B12), 2363, doi:10.1029/2002JB001942.

Atwater, T., and J. Stock (1998), Pacific-North America plate tectonics of the Neogene southwestern United States: An update, *Int. Geol. Rev.*, *40*(5), 375–402.

Blanpied, M. L., T. E. Tullis, and J. D. Weeks (1998), Effects of slip, slip rate, and shear heating on the friction of granite, *J. Geophys. Res.*, *103*(B1), 489–511.

Blythe, A. E., M. A. d'Alessio, and R. Bürgmann (2004), Constraining the exhumation and burial history of the SAFOD pilot hole with apatite fission track and (U-Th)/He thermochronometry, *Geophys. Res. Lett.*, *31*, L15S16, doi:10.1029/2003GL019407.

Brocher, T. M., T. Parsons, A. M. Trehu, C. M. Snelson, and M. A. Fisher (2003), Seismic evidence for widespread serpentinized forearc upper mantle along the Cascadia margin, *Geology*, *31*(3), 267–270.

Brodsky, E. E., and H. Kanamori (2001), Elastohydrodynamic lubrication of faults, *J. Geophys. Res.*, *106*(B8), 16,357–16,374.

Brown, K. M., A. Kopf, M. B. Underwood, and J. L. Weinberger (2003), Compositional and fluid pressure controls on the state of stress on the nankai subduction thrust: A weak plate boundary, *Earth Planet. Sci. Lett.*, *214*(3–4), 589–603.

Brune, J. N. (2002), Heat flow on the creeping section of the San Andreas fault: A localized transient perspective, *Eos Trans. AGU*, *83*(47), Fall Meet. Suppl., Abstract S21A-0979.

Brune, J. N., and W. Thatcher (2002), Strength and energetics of active fault zones, in *International Handbook of Earthquake and Engineering Seismology*, *Int. Geophys. Ser.*, vol. 81A, edited by W. H. K. Lee et al., pp. 569–588, Elsevier, New York.

Brune, J. N., T. L. Henyey, and R. F. Roy (1969), Heat flow, stress, and rate of slip along the San Andreas fault, California, *J. Geophys. Res.*, *74*(15), 3821–3827.

Brune, J. N., S. Brown, and P. Johnson (1993), Rupture mechanism and interface separation in foam rubber models of earthquakes: A possible solution to the heat flow paradox and the paradox of large overthrusts, *Tectonophysics*, *218*, 59–67.

Byerlee, J. D. (1978), Friction of rocks, *Pure Appl. Geophys.*, *116*(4), 615–626.

Camacho, A., I. McDougall, R. Armstrong, and J. Braun (2001), Evidence for shear heating, Musgrave block, central Australia, *J. Struct. Geol.*, *23*(6–7), 1007–1013.

Castillo, D., and S. H. Hickman (2000), Systematic near-field stress rotations adjacent to the Carrizo Plain segment of the San Andreas fault, in *Proceedings of the 3rd Conference on Tectonic Problems of the San Andreas Fault System*, vol. XXI, edited by G. Bokelmann and R. Kovach, pp. 252–254, Stanford Univ. Press, Stanford, Calif.

d'Alessio, M. A., A. E. Blythe, and R. Bürgmann (2003), No frictional heat along the San Gabriel fault, California: Evidence from fission-track thermochronology, *Geology*, *31*(6), 541–544.

Evans, J. P., M. J. Rymer, and D. Moore (2004), Microstrutural analyses of an exhumed part of the San Andreas fault near the SAFOD site, California, *Eos Trans. AGU*, *85*(47), Fall Meet. Suppl., Abstract T13A-1337.

Forsyth, D. W., and B. Wilson (1984), Three-dimensional temperature structure of a ridge-transform-ridge system, *Earth Planet. Sci. Lett.*, *70*(2), 355–362.

Fulton, P. M., D. M. Saffer, R. N. Harris, and B. A. Bekins (2004), Re-evaluation of heat flow data near Parkfield, CA: Evidence for a weak San Andreas Fault, *Geophys. Res. Lett.*, *31*, L15S15, doi:10.1029/2003GL019378.

Guzofski, C. A., and K. P. Furlong (2002), Migration of the Mendocino triple junction and ephemeral crustal deformation: Implications for California Coast range heat flow, *Geophys. Res. Lett.*, *29*(1), 1012, doi:10.1029/2001GL013614.

Hardebeck, J., and E. Hauksson (1999), Role of fluids in faulting inferred from stress field signatures, *Science*, *285*, 236–239.

Hardebeck, J. L., and A. J. Michael (2004), Stress orientations at intermediate angles to the San Andreas Fault, California, *J. Geophys. Res.*, *109*, B11303, doi:10.1029/2004JB003239.

Harris, R. A. (1998), Introduction to special section: Stress triggers, stress shadows, and implications for seismic hazard, *J. Geophys. Res.*, *103*(B10), 24,347–24,358.

Henyey, T. L. (1968), Heat flow near major strike-slip faults in central and southern California, Ph.D. thesis, Calif. Inst. of Technol., Pasadena, Calif.

Hickman, S., and M. Zoback (2004), Stress orientations and magnitudes in the SAFOD pilot hole, *Geophys. Res. Lett.*, *31*, L15S12, doi:10.1029/2004GL020043.

Irwin, W. P., and I. Barnes (1975), Effect of geologic structure and metamorphic fluids on seismic behavior of the San Andreas fault system in central and northern California, *Geology*, *3*(12), 713–716.

Jachens, R. C., C. M. Wentworth, and R. J. McLaughlin (1998), Pre-San Andreas location of the Gualala block inferred from magnetic and gravity anomalies, in *Geology and tectonics of the Gualala block, northern California, Book 84*, edited by W. P. Elder, pp. 27–63, Pac. Sect., Soc. of Sediment. Geol., Fullerton, Calif.

Lachenbruch, A. H. (1980), Frictional heating, fluid pressure, and the resistance to fault motion, *J. Geophys. Res.*, *85*(B11), 6097–6112.

Lachenbruch, A. H. (1986), Simple models for the estimation and measurement of frictional heating by an earthquake, *U.S. Geol. Surv. Open File Rep.*, *86-508*, 1–13.

Lachenbruch, A. H., and J. H. Sass (1973), Thermo-mechanical aspects of the San Andreas fault system, in *Proceedings of the Conference on Tectonic Problems of the San Andreas Fault System*, pp. 192–205, Stanford Univ. Press, Stanford, Calif.

Lachenbruch, A. H., and J. H. Sass (1980), Heat flow and energetics of the San Andreas fault zone, *J. Geophys. Res.*, *85*(B11), 6185–6222.

Lachenbruch, A. H., and J. H. Sass (1981), Corrections to "heat flow and energetics of the San Andreas fault zone" and some additional comments on the relation between fault friction and observed heat flow, *J. Geophys. Res.*, *86*(B8), 7171–7172.

Leloup, P. H., Y. Ricard, J. Battaglia, and R. Lacassin (1999), Shear heating in continental strike-slip shear zones: Model and field examples, *Geophys. J. Int.*, *136*(1), 19–40.

Lockner, D. A., and N. M. Beeler (2002), Rock failure and earthquakes, in *International Handbook of Earthquake and Engineering Seismology*, *Int. Geophys. Ser.*, vol. 81A, edited by W. H. K. Lee et al., pp. 505–537, Elsevier, New York.

Lockner, D. A., and P. G. Okubo (1983), Measurements of frictional heating in granite, *J. Geophys. Res.*, *88*(B5), 4313–4320.

Mase, C. W., and L. Smith (1987), Effects of frictional heating on the thermal, hydrologic, and mechanical response of a fault, *J. Geophys. Res.*, *92*(B7), 6249–6272.

McGarr, A. F. (1999), On relating apparent stress to the stress causing earthquake fault slip, *J. Geophys. Res.*, *104*(B2), 3003–3011.

McKenzie, D., and J. N. Brune (1972), Melting on fault planes during large earthquakes, *Geophys. J. R. Astron. Soc.*, *29*, 65–78.

Melosh, H. J. (1996), Dynamical weakening of faults by acoustic fluidization, *Nature*, *379*(6566), 601–606.

Moore, D. E., D. A. Lockner, R. Summers, M. Shengli, and J. D. Byerlee (1996), Strength of chrysotile-serpentinite gouge under hydrothermal conditions: Can it explain a weak San Andreas fault?, *Geology*, *24*(11), 1041–1044.

Moore, D. E., D. A. Lockner, H. Tanaka, and K. Iwata (2004), The coefficient of friction of chrysotile gouge at seismogenic depths, *Int. Geol. Rev.*, *46*(5), 385–398.

Morrow, C., B. Radney, and J. D. Byerlee (1992), Frictional strength and the effective pressure law of montmorillonite and illite clays, in *Fault Mechanics and Transport Properties of Rocks*, edited by T.-F. Wong and B. Evans, pp. 69–88, Elsevier, New York.

Mount, V. S., and J. Suppe (1987), State of stress near the San Andreas fault, *Geology*, *15*(12), 1143–1146.

Murakami, M., T. Tagami, and N. Hasebe (2002), Ancient thermal anomaly of an active fault system: Zircon fission-track evidence from Nojima GSJ 750 m borehole samples, *Geophys. Res. Lett.*, *29*(23), 2123, doi:10.1029/2002GL015679.

Murray, J. R., P. Segall, P. Cervelli, W. Prescott, and J. Svarc (2001), Inversion of GPS data for spatially variable slip-rate on the San Andreas fault near Parkfield, CA, *Geophys. Res. Lett.*, *28*(2), 359–362.

O'Neil, J. R., and T. C. Hanks (1980), Geochemical evidence for water-rock interaction along the San Andreas and Garlock faults of California, *J. Geophys. Res.*, *85*(B11), 6286–6292.

Provost, A.-S., and H. Houston (2001), Orientation of the stress field surrounding the creeping section of the San Andreas fault: Evidence for a narrow mechanically weak fault zone, *J. Geophys. Res.*, *106*(B6), 11,373–311,386.

Provost, A., and H. Houston (2003), Stress orientations in northern and central California: Evidence for the evolution of frictional strength along the San Andreas plate boundary system, *J. Geophys. Res.*, *108*(B3), 2175, doi:10.1029/2001JB001123.

Rice, J. R. (1992), Fault stress states, pore pressure distributions, and the weakness of the San Andreas fault, in *Fault Mechanics and Transport Properties of Rocks*, edited by T.-F. Wong and B. Evans, pp. 475–503, Elsevier, New York.

Rolandone, F., and C. Jaupart (2002), The distribution of slip rate and ductile deformation in a strike-slip shear zone, *Geophys. J. Int.*, *148*, 179–192.

Rymer, M. J., R. D. Catchings, M. Thayer, and J. R. Arrowsmith (2004), Structure of the San Andreas fault zone and SAFOD drill site as revealed by surface geologic mapping and seismic profiling near Parkfield, California, *Eos Trans. AGU*, *85*(47), Fall Meet. Suppl., Abstract T11F-08.

Saffer, D. M., B. A. Bekins, and S. Hickman (2003), Topographically driven groundwater flow and the San Andreas heat flow paradox revisited, *J. Geophys. Res.*, *108*(B5), 2274, doi:10.1029/2002JB001849.

Scholz, C. H. (1998), Earthquakes and friction laws, *Nature*, *391*(1), 37–42.

Scholz, C. H. (2000), Evidence for a strong San Andreas fault, *Geology*, *28*(2), 163–166.

Scholz, C. H., and T. C. Hanks (2004), The strength of the San Andreas fault: A discussion, in *Rheology and Deformation of the Lithosphere at Continental Margins*, edited by G. D. Karner et al., pp. 261–283, Columbia Univ. Press, New York.

Scholz, C. H., J. Beavan, and T. C. Hanks (1979), Metamorphism, argon depletion, heat flow and stress on the Alpine fault, in *Proceedings of Conference VIII: Analysis of Actual Fault Zones in Bedrock*, *U.S. Geol. Surv. Open File Rep.*, *79-1239*, 534–586.

Sims, J. D. (1993), Chronology of displacement on the San Andreas fault in central California: Evidence from reversed positions of exotic rock bodies near Parkfield, CA, in *The San Andreas Fault System: Displacement, Palinspastic Reconstruction, and Geologic Evolution*, edited by R. E. Powell, R. J. I. Weldon, and J. C. Matti, *Mem. Geol. Soc. Am.*, *178*, 231–256.

ten Brink, U. S., N. Shimizu, and P. C. Molzer (1999), Plate deformation at depth under northern California: Slab gap or stretched slab?, *Tectonics*, *18*(6), 1084–1098.

Thatcher, W., and P. C. England (1998), Ductile shear zones beneath strike-slip faults: Implications for the thermomechanics of the San Andreas fault zone, *J. Geophys. Res.*, *103*(B1), 891–905.

Titus, S. J., C. DeMets, and B. Tikoff (2005), New slip rate estimates for the creeping segment of the San Andreas fault, California, *Geology*, *33*(3), 205–208.

Townend, J., and M. D. Zoback (2000), How faulting keeps the crust strong, *Geology*, *28*, 399–402.

Townend, J., and M. D. Zoback (2004), Regional tectonic stress near the San Andreas fault in central and southern California, *Geophys. Res. Lett.*, *31*, L15S11, doi:10.1029/2003GL018918.

Williams, C. F., and T. N. Narasimhan (1989), Hydrogeologic constraints on heat-flow along the San Andreas fault—A testing of hypotheses, *Earth Planet. Sci. Lett.*, *92*(2), 131–143.

Williams, C. F., F. V. Grubb, and S. P. Galanis Jr. (2004), Heat flow in the SAFOD pilot hole and implications for the strength of the San Andreas Fault, *Geophys. Res. Lett.*, *31*, L15S14, doi:10.1029/2003GL019352.

Xu, G., and P. J. J. Kamp (2000), Tectonics and denudation adjacent to the Xianshuihe fault, eastern Tibetan Plateau: Constraints from fission track thermochronology, *J. Geophys. Res.*, *105*(B8), 19,231–19,251.

R. Bürgmann, Department of Earth and Planetary Science, University of California, Berkeley, CA 94720-4767, USA.

M. A. d'Alessio and C. F. Williams, U.S. Geological Survey, 345 Middlefield Road, MS 977, Menlo Park, CA 94025, USA. (dalessio@usgs.gov)